Supporting Information

Enhancing CO_2 Electroreduction with Decamethylcucurbit[5]uril-Alkaline Earth Metal Modified Pd Nanoparticles

Tao Shao, [a, b] Xianmeng Song, [b] Zongnan Wei, [b] Shuaibing Yang, [b] siying zhang, [a, b] Rong Cao [b, c] and Minna Cao [*b, c]

[a] College of Chemistry and Materials Science, Fujian Normal University, Fuzhou 350007, P. R. China.

[b] State Key Laboratory of Structural Chemistry, Fujian Institute of Research on the Structure of Matter, Chinese Academy Sciences, Fuzhou, Fujian, 350002, P. R. China.

[c] University of Chinese Academy of Sciences, Beijing, 100049, P. R. China.

*E-mail address: mncao@fjirsm.ac.cn (M. Cao)

Supplementary Index

Experimental section

Fig. S18 Schematic illustration of operando electrochemical ATR-FTIR measurement.

Fig. S19 Operando ATR-FTIR spectra of $Me_{10}CB[5]$-M/Pd collected at -0.7 V vs. RHE under CO_2-saturated 0.5 M $KHCO_3$ electrolyte.

Table S1: Crystallographic Data for $Me_{10}CB[5]$-M/[$PdCl_4$].

Table S2: Different valence distribution of Pd for $Me_{10}CB[5]$-M/Pd.

Table S3: Detail Inductive Coupled Plasma (ICP) data of Pd for $Me_{10}CB[5]$-M/Pd.

Table S4: Detail information of EIS fitting data for $Me_{10}CB[5]$-M/Pd.

Table S5: Summary of the performances of Pd-based electrocatalysts for electrochemical CO_2RR in H-type cells.

EXPERIMENTAL SECTION

Chemicals. All reagents and chemicals were obtained commercially and used without further purification. Urea was provided by Alfa Aesar. Palladium chloride ($PdCl_2$), concentrated hydrochloric acid (HCl), cadmium chloride ($CdCl_2$), strontium chloride ($SrCl_2$), calcium chloride ($CaCl_2$), Potassium bicarbonate ($KHCO_3$), and Sulfuric Acid were provided by Sinopharm Chemical Reagent Co. Ltd (China). Vulcan XC-72R carbon black was purchased from Cabot Corp. Nafion solution (5wt%) was purchased from Sigma-Aldrich. All solutions were prepared with ultrapure water with a resistivity of 18.25 MΩ cm was used to prepare all solutions. Decamethylcucurbit[5]uril ($Me_{10}CB[5]$) was synthesized according to the previous literature.[1]

Preparation of supramolecular self-assembly precursors: The supramolecular self-assembly precursors were synthesized via the liquid phase diffusion method at room temperature. 0.17 mmol $PdCl_2$ and 1 mL of HCl (6 M) were dissolved in 20 mL deionized water to prepare solution I. 0.1 mmol $Me_{10}CB[5]$ and 0.1 mmol MCl_2 (M=Sr, Ca, Cd) were dissolved in 20 mL hydrochloric acid solution (1 mL 6 M of HCl in 19 mL of deionized water) to get solution II. Solution I and II were carefully transferred to two sides of the H-tube. Brown crystals were obtained through slow diffusion after 48 hours in the H-tube. The synthesis of $Me_{10}CB[5]$-Ca/[$PdCl_4$] and $Me_{10}CB[5]$-Cd/[$PdCl_4$] were similar to that of $Me_{10}CB[5]$-Sr/[$PdCl_4$] except

$SrCl_2$ were adjusted to $CaCl_2$ or $CdCl_2$.

(1) **Me_{10}CB[5]-Sr/[$PdCl_4$] (CCDC 2301984)**

Elemental analysis calculated (%) for $C_{40}H_{74}Cl_4N_{20}O_{22}PdSr$: C, 31.53%; H, 4.86%; N, 18.39%. Found: C, 30.46; H, 4.16%; N, 17.46%.

(2) **Me_{10}CB[5]-Ca/[$PdCl_4$] (CCDC 2301985)**

Elemental analysis calculated (%) for $C_{80}H_{100}Cl_{21}N_{40}O_{20}Pd_4Ca_4$: C, 29.33%; H, 3.05%; N, 17.11%. Found: C, 28.94%; H, 4.35%; N, 16.84%.

(3) **Me_{10}CB[5]-Cd/[$PdCl_4$] (CCDC 2301986)**

Elemental analysis calculated (%) for $C_{40}H_{58}Cl_5N_{20}O_{13.65}PdCd$: C, 33.48%; H, 4.04%; N, 19.53%. Found: C, 31.99%; H, 4.14%; N, 18.03%..

Preparation of Pd-based NPs: The Pd-based NPs were synthesized via thermal reduction. First, the blocks of crystals were ground into powder and loaded into a porcelain boat. Then, the boat was placed into a tube furnace under a 5% H_2/95% N_2 atmosphere at a rate of 5 ℃ min^{-1} to 300 ℃ and maintained for 5 hours to prepare Me_{10}CB[5]-M/Pd NPs.

Characterization: Single crystal X-ray diffraction (SCXRD) was performed on a Bruker D8 Venture diffractometer equipped with Mo-Kα radiation (λ = 0.71073 Å). Crystal data and structure refinement parameters are given in Table S1. CCDC 2301984 - 2301986 contains supplementary crystallographic data for this paper. These data can be obtained free of charge from the Cambridge Crystallographic Data Centre. Power X-ray diffraction (PXRD) patterns were performed with a Rigaku

Mini Flex 600 diffractometer with a Cu Kα radiation source (λ = 1.5418Å) at a low scanning speed of 1° min^{-1}. Fourier transform infrared (FT-IR) spectroscopy was performed by Lambda900. Thermal gravimetric analysis (TGA) was performed using the TA SDT-Q600 instrument, with a heating rate of 10°C min^{-1} under the flow of nitrogen atmosphere. Transmission electron microscopy (TEM), high-resolution transmission electron microscopy (HR-TEM), high-angle annular dark-field scanning TEM (HAADF-STEM), and energy dispersive X-ray spectroscopy analysis (EDX) measurements were performed using FEI Tecnai G2 F20 electron microscope. Elemental analysis (EA) was carried out on the Elementar Vario EL III analyzer. The gas isotherms of the samples were measured using an ASAP 2020 from Micromeritics Co. Ltd. X-ray photoelectron spectroscopy (XPS) measurements were performed on an ESCALAB 250Xi X-ray photoelectron spectrometer (Thermo Fisher) using an Al Kα source (15 KV, 10 mA). The Pd loading amount was determined using an inductively coupled plasma emission spectrometer (ICP) Jobin Yvon Ultima 2. All the electrochemical experiments were performed on the CHI600E electrochemical workstation. The gas-phase products were detected using a gas chromatograph (GC) (Agilent 7820A), while liquid-phase products were detected by ion-exchange chromatography (IC) (Metrohm China Limited).

Electrochemical measurement: The electrochemical measurements

were carried out on a CHI 600E electrochemical workstation using a standard three-electrode configuration within an H-cell. Here, 35 mL of 0.5 M $KHCO_3$ solution was used as the electrolyte in the anode and cathode compartments of the two sides of the H-cell, respectively. The Ag/AgCl electrodes (Gaoss Union, saturated KCl) and Pt net (1cm^2) were used as the reference and counter electrodes. Then, dispersing 6 mg Pd-based catalysts with the same quality Vulcan XC-72R carbon black in a mixed solution of 0.04 mL Nafion (5 wt %) and 0.96 mL isopropanol by ultrasonic treating for 2 hours to get the ink of Pd-based catalysts. The working electrode was a carbon fiber paper (1 cm^2) coated by the ink. The volume of catalyst ink taken depended on the mass fraction of Pd in different catalysts. Loading to the metal of Pd was 90 μg cm^{-2}, and then the as-prepared working electrode was dried at room temperature.

Cycle voltammetry (CV) was used to clean the catalyst's surface. Then, linearly scanned volts (LSVs) were recorded with the scan rate of 10 mV s^{-1} in N_2-saturated 0.5 M $KHCO_3$ (pH=8.5) solution and CO_2-saturated 0.5 M $KHCO_3$ (pH=7.2) solution, respectively. CO_2 gas continuously flew into the cathodic electrolyte during CO_2RR. The CO_2 gas flow rate was controlled using a mass flow meter and adjusting it to 30 mL min^{-1}. After at least 10 minutes of electrolysis, 1 mL of gas was taken by sampling needle and quantified by gas chromatography (GC). After 150 min of electrolysis at each potential, the liquid products were collected and

analyzed by ion chromatography (IC).

The Faradaic efficiency of a particular gas product was calculated by the equation:

$$FE = \frac{Pv}{RT} \times \frac{mcF \times 10^{-6}(m^3 / mL)}{1 \times 60(s / \min)}$$

c (ppm): volume concentration of particular gas product in the exhaust gas from the cell;

v: gas flow rate measured by a flow meter, 30 mL min^{-1}

I: total steady-state cell current;

m: the electron transfer number for product formation;

F: Faradaic constant 96485 C mol^{-1};

P: one atmosphere, 1.013×10^5 Pa;

R: universal gas constant, 8.314 J mol^{-1} K^{-1};

T: room temperature, 298.15 K.

All the electrochemical measurements mentioned in this article were without resistance compensation. All the potentials reported in this article were converted to the reversible hydrogen electrode (RHE) using the equation:

$$E_{RHE} = E_{Ag/AgCl} + 0.197V + 0.0591 \times pH$$

The Operando Electrochemical ATR-FTIR measurement: Operando electrochemical ATR-FTIR spectroscopy was performed using a Nicolet 6700 spectrometer (Thermo Fisher) equipped with a liquid nitrogen-cooled MCT detector and a Ge single crystal infrared window. A specific

Teflon electrolytic cell was used for the measurements, as shown in Fig. S18†. The working electrode was a glassy carbon electrode coated with the catalyst (10 µL). A platinum mesh electrode (1 cm^2) and an Ag/AgCl (Gaoss Union, saturated KCl) were used as the counter electrode and reference electrode, respectively. The ATR-FTIR results of $Me_{10}CB[5]$-M/Pd were recorded in a CO_2-saturated 0.5 M $KHCO_3$ solution at -0.7 V vs. RHE. Additionally, spectra of $Me_{10}CB[5]$-M/Pd were collected at 10 s, 30 s, 60 s, and 5 min intervals to explore differences in the CO_2RR mechanism. (All spectra were subtracted with the background subtraction.)

References:

1. A. Flinn, G. C. Hough, J. F. Stoddart, and D. J. Williams, Decamethylcucurbit[5]uril, *Angew. Chem. Int. Ed.*, 1992, **31**, 1475-1477.

Supplementary Figure

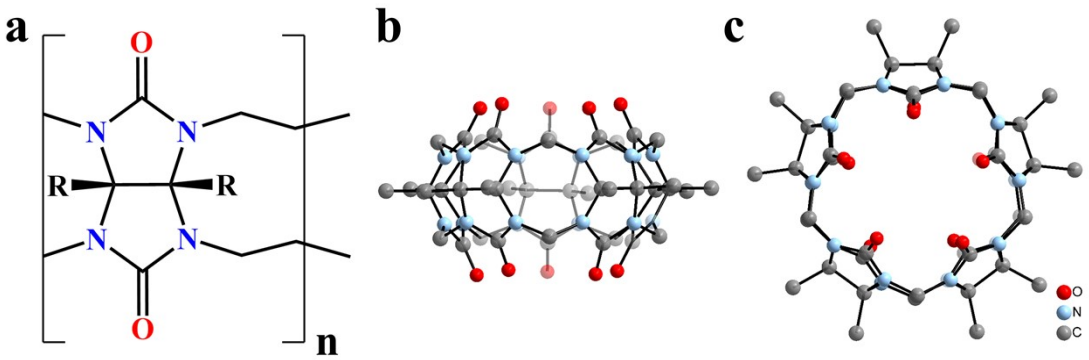

Fig. S1 (a) Structural presentation of CB[n]s (n=5-8, 10, 14, and R=H or CH_3), (b)side, and (c) top view of $Me_{10}CB[5]$.

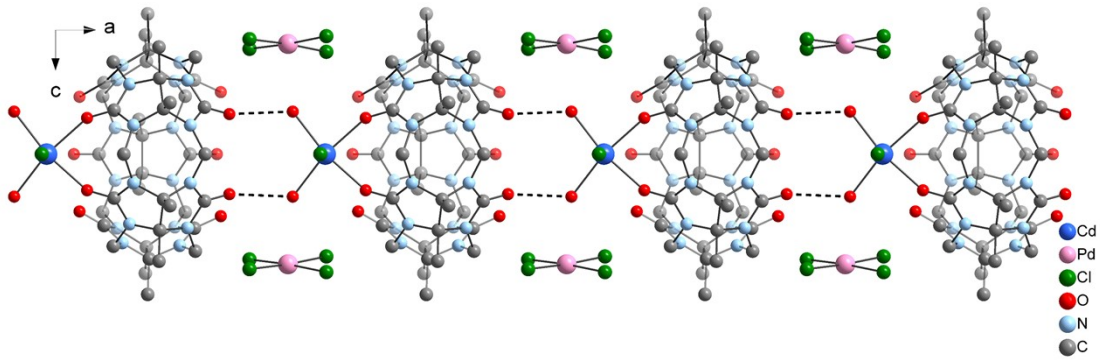

Fig. S2 A view of the packing pattern of compound $Me_{10}CB[5]$-Sr/$[PdCl_4]$.

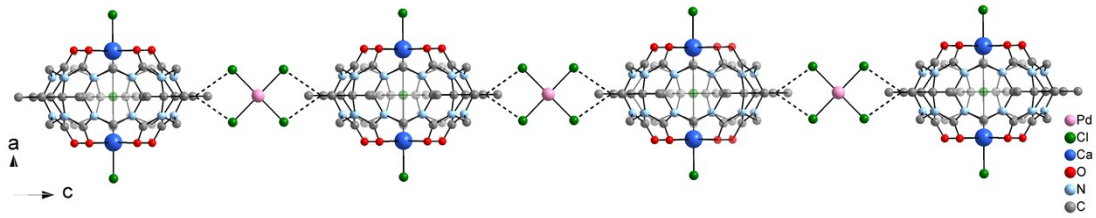

Fig. S3 A view of the packing pattern of compound $Me_{10}CB[5]$-Ca/$[PdCl_4]$.

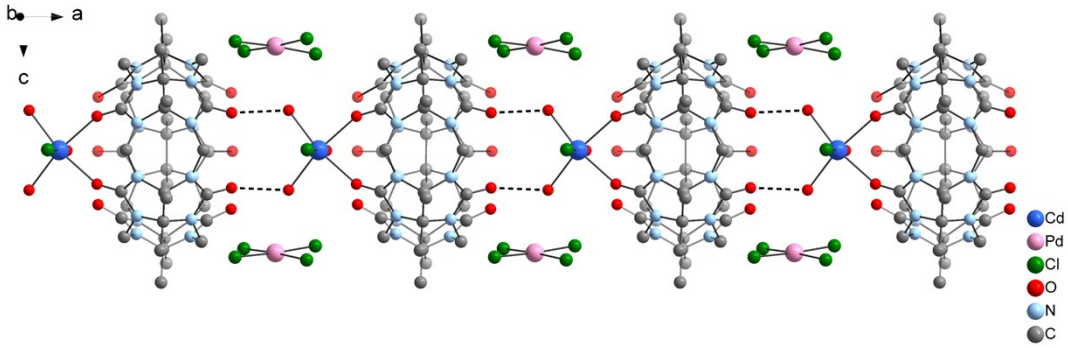

Fig. S4 A view of the packing pattern of compound $Me_{10}CB[5]$-Cd/[$PdCl_4$].

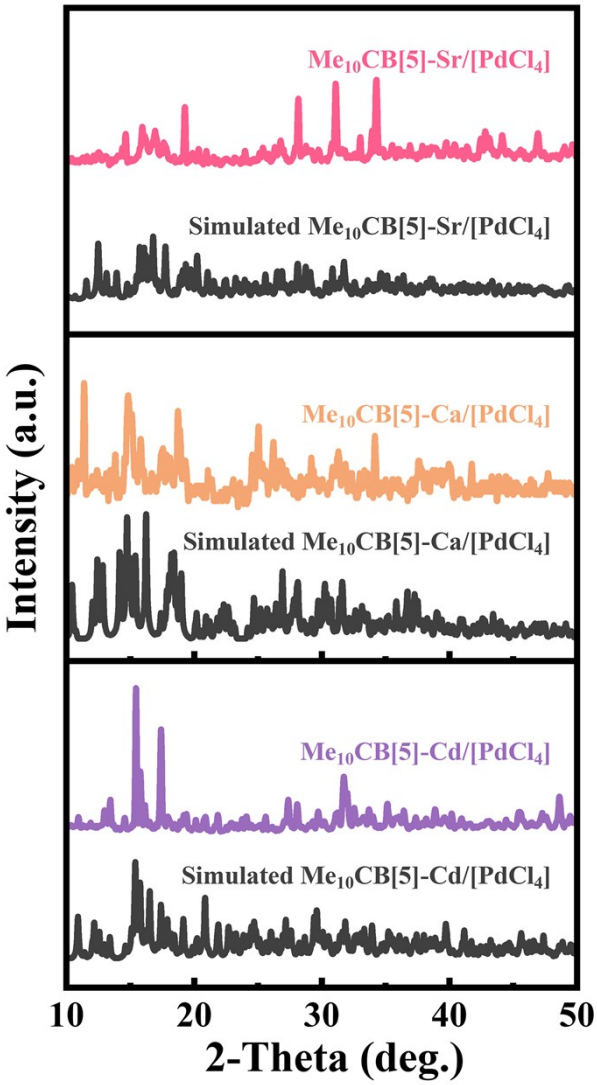

Fig. S5 XRD patterns of $Me_{10}CB[5]$-M/[$PdCl_4$].

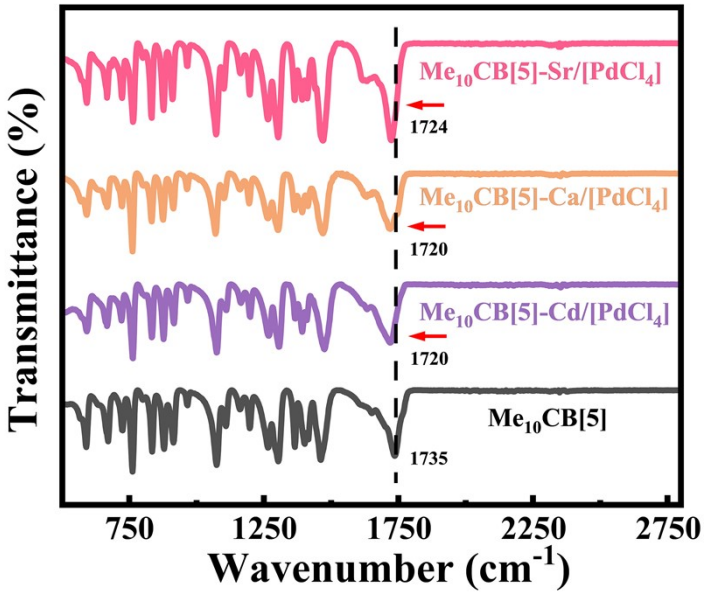

Fig. S6 FT-IR curves of $Me_{10}CB[5]$-M/[$PdCl_4$], and $Me_{10}CB[5]$.

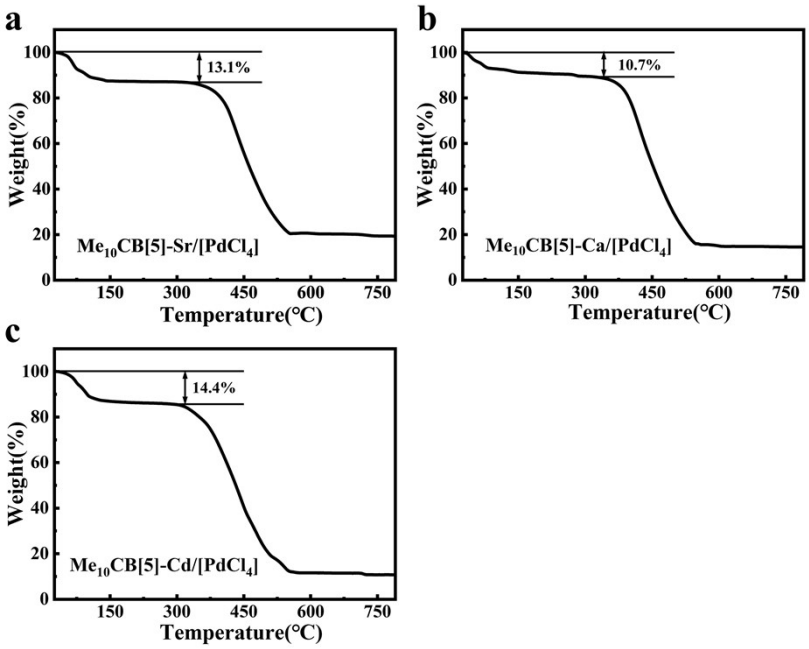

Fig. S7 TGA curves of $Me_{10}CB[5]$-M/[$PdCl_4$], (M=Sr, Ca, and Cd).

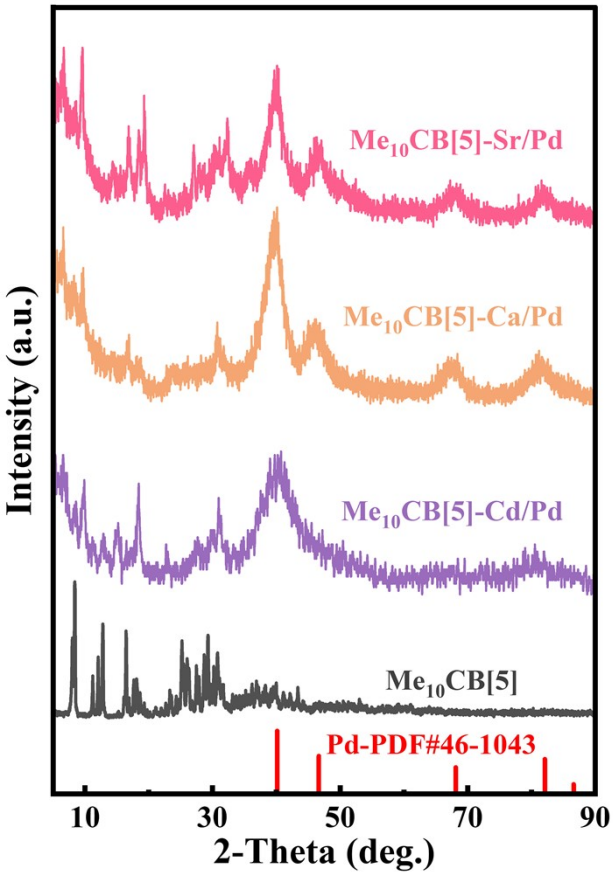

Fig. S8 PXRD patterns of $Me_{10}CB[5]$-M/Pd (M=Sr, Ca and Cd) and $Me_{10}CB[5]$.

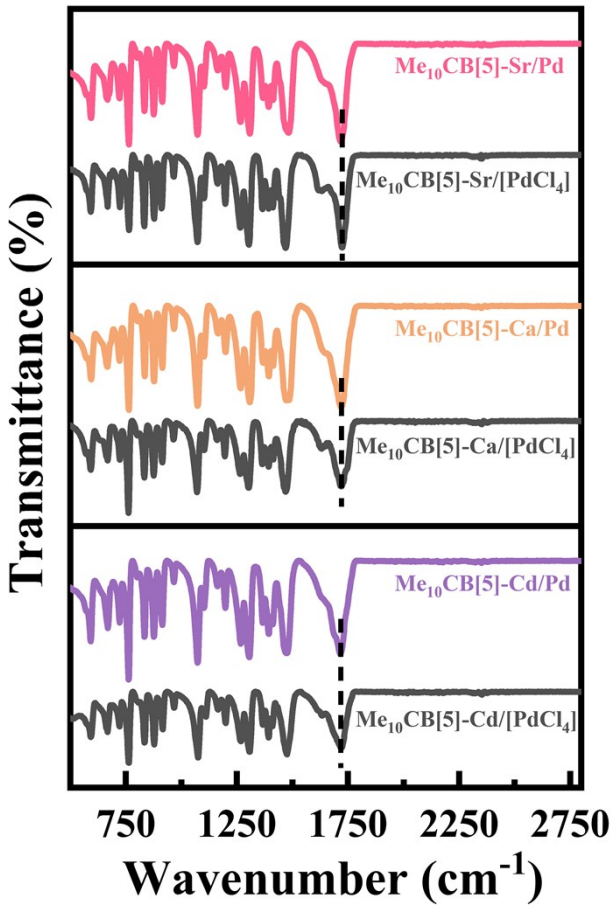

Fig. S9 FT-IR curves of $Me_{10}CB[5]$-M/[$PdCl_4$], and $Me_{10}CB[5]$-M/Pd.

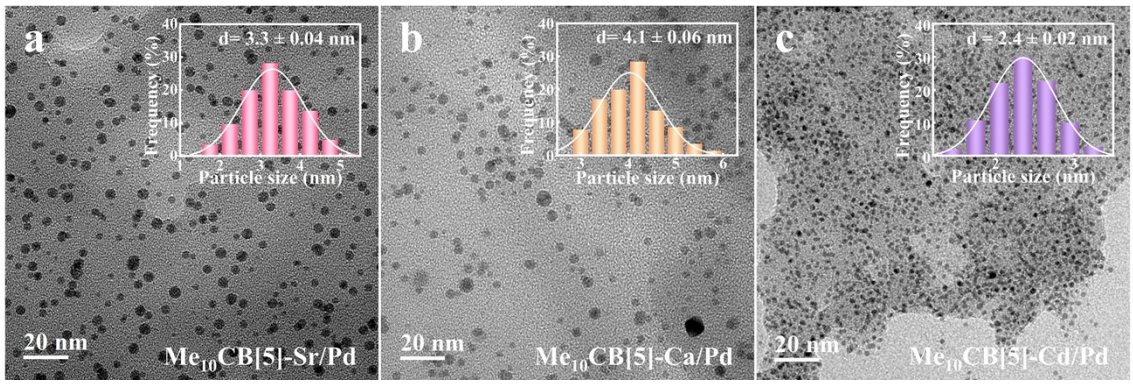

Fig. S10 The TEM images and particle-size distribution of (a) $Me_{10}CB[5]$-Sr/Pd, (b) $Me_{10}CB[5]$-Ca/Pd, (c) $Me_{10}CB[5]$-Cd/Pd.

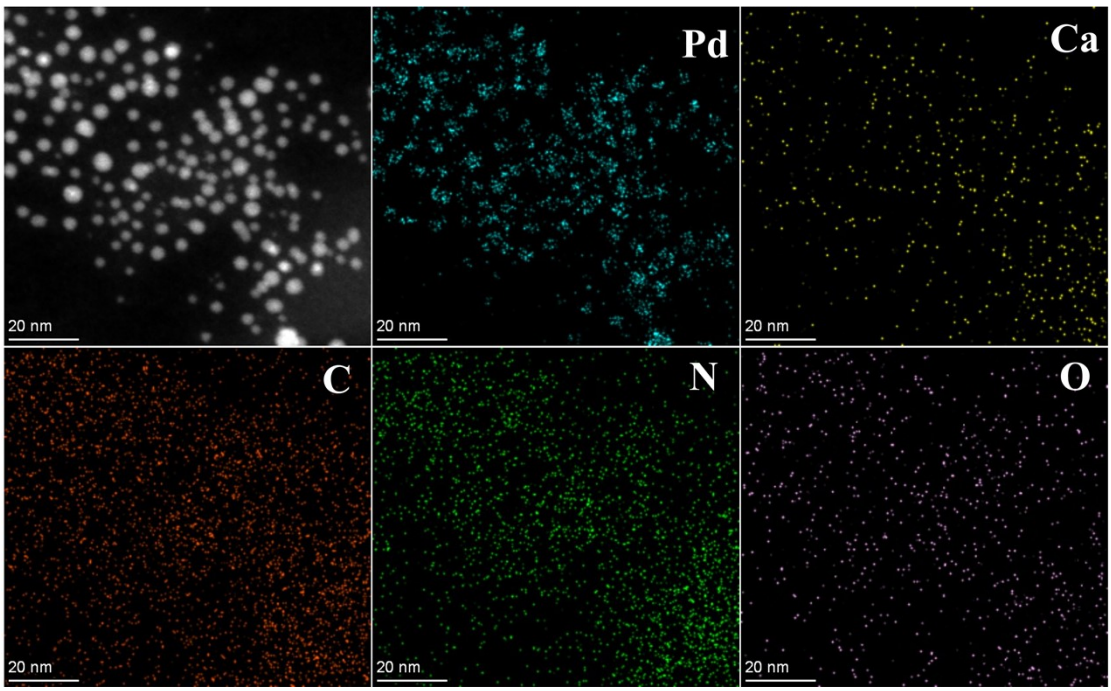

Fig. S11 HAADF-STEM image, and the corresponding EDX mappings of Pd (blue), Ca (yellow), C (orange), N (green), and O (purple) for $Me_{10}CB[5]$-Ca/Pd.

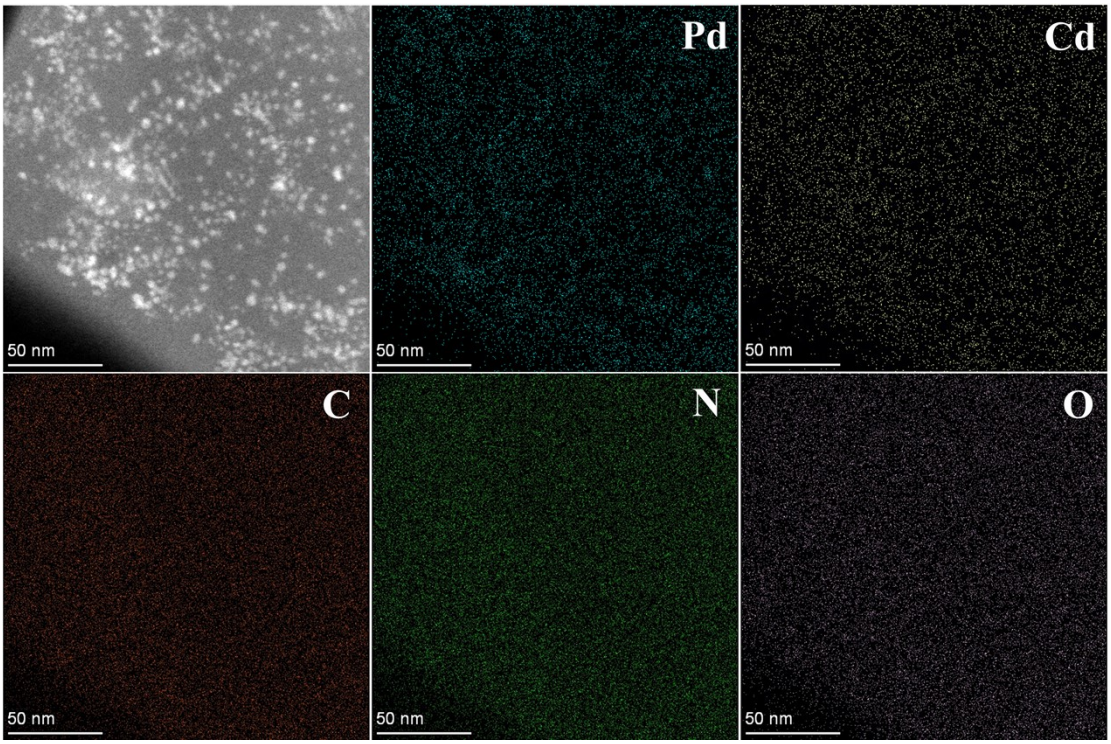

Fig. S12 HAADF-STEM image, and the corresponding EDX mappings of Pd (blue), Cd (yellow), C (orange), N (green), and O (purple) for $Me_{10}CB[5]$-Cd/Pd.

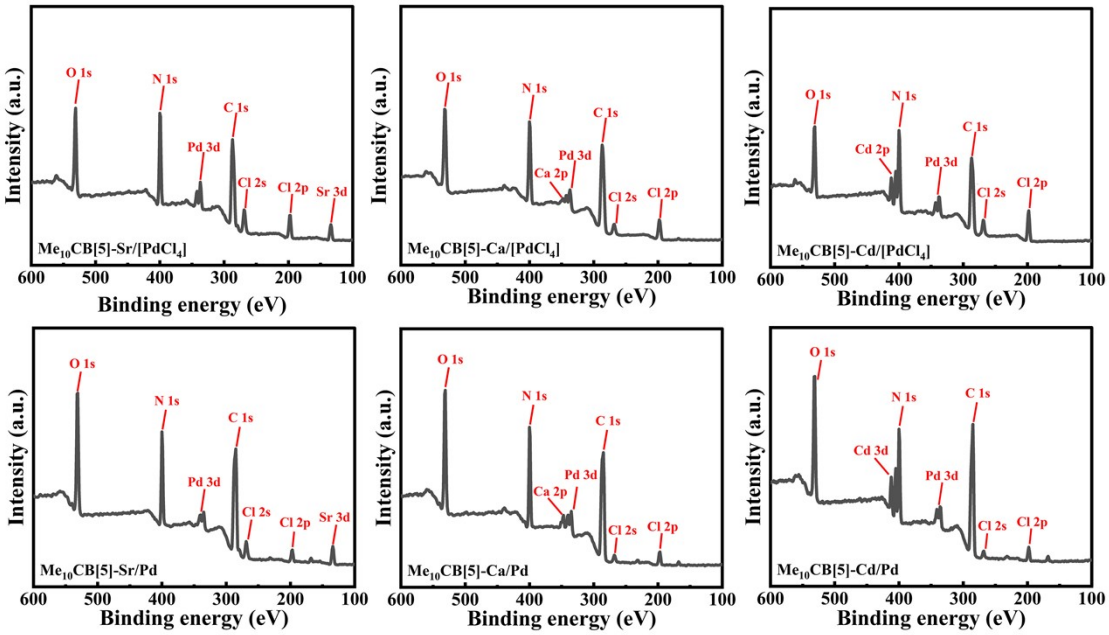

Fig. S13 XPS survey spectrum of $Me_{10}CB[5]$-M/[$PdCl_4$], and $Me_{10}CB[5]$-M/Pd (M=Sr, Ca, and Cd).

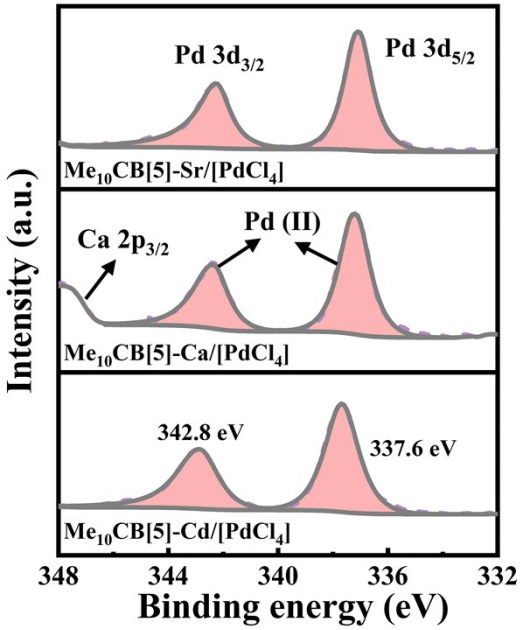

Fig. S14 The Pd 3d high-resolution spectrum of $Me_{10}CB[5]$-M/[$PdCl_4$] (M=Sr, Ca, and Cd).

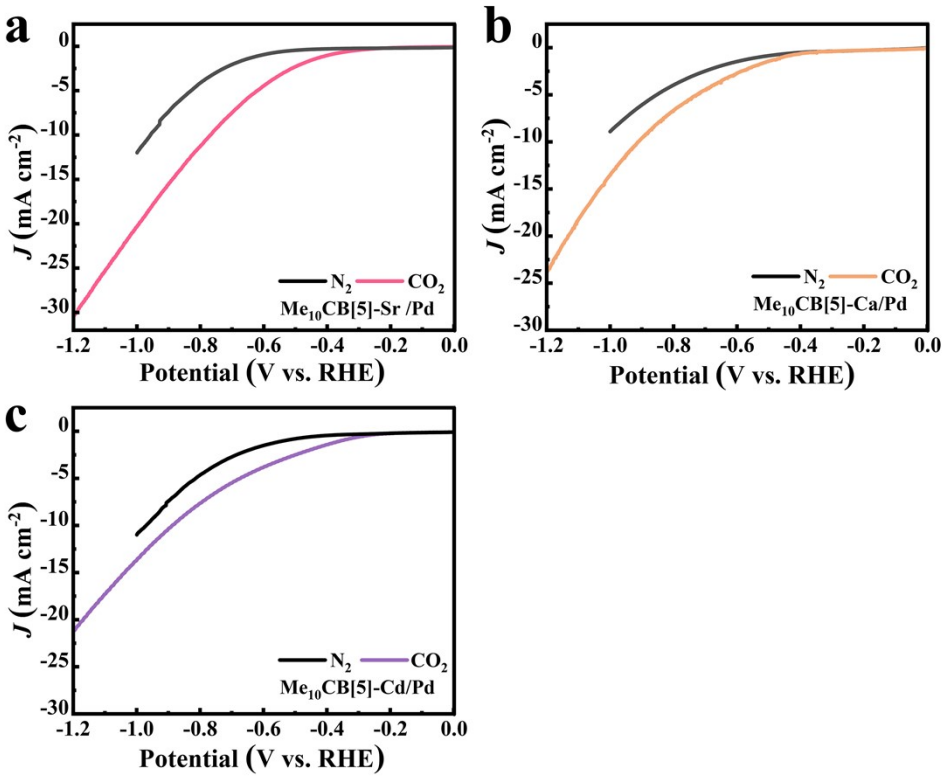

Fig. S15 The linear sweep voltammetry of (a) $Me_{10}CB[5]$-Sr/Pd, (b) $Me_{10}CB[5]$-Ca/Pd, and (c) $Me_{10}CB[5]$-Cd/Pd in N_2-saturated 0.5 M $KHCO_3$ (pH = 8.2, black), the current density in CO_2-saturated electrolyte increases significantly (pH = 7.2, colors).

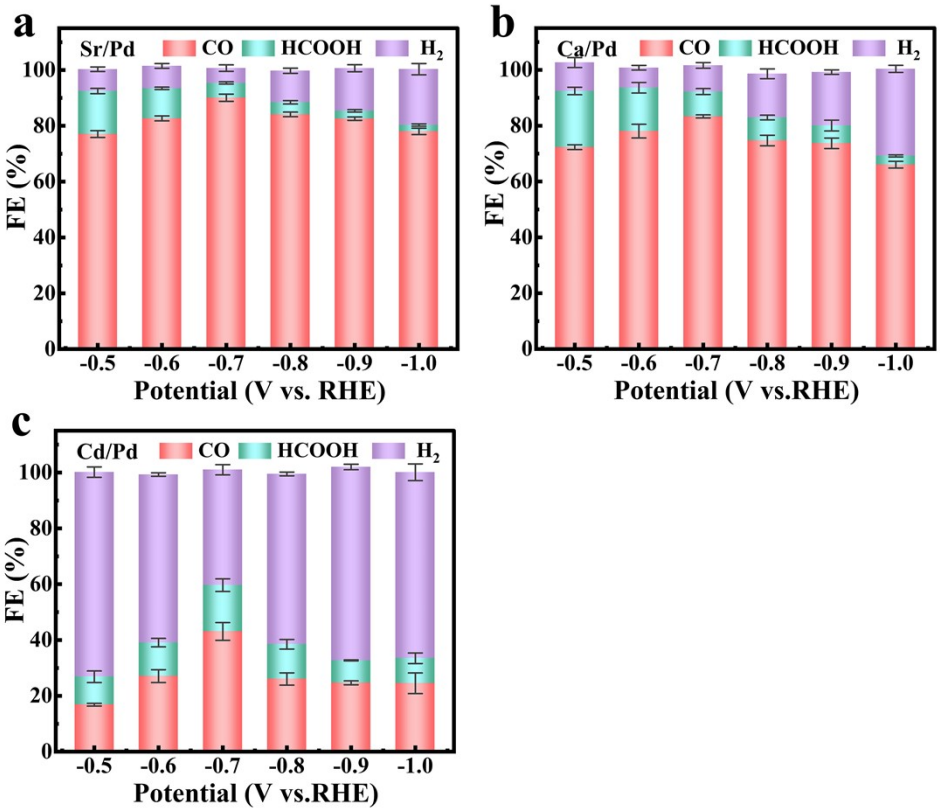

Fig. S16 The Faradaic efficiencies of (a) $Me_{10}CB[5]$-Sr/Pd, (b) $Me_{10}CB[5]$-Ca/Pd and (c) $Me_{10}CB[5]$-Cd/Pd.

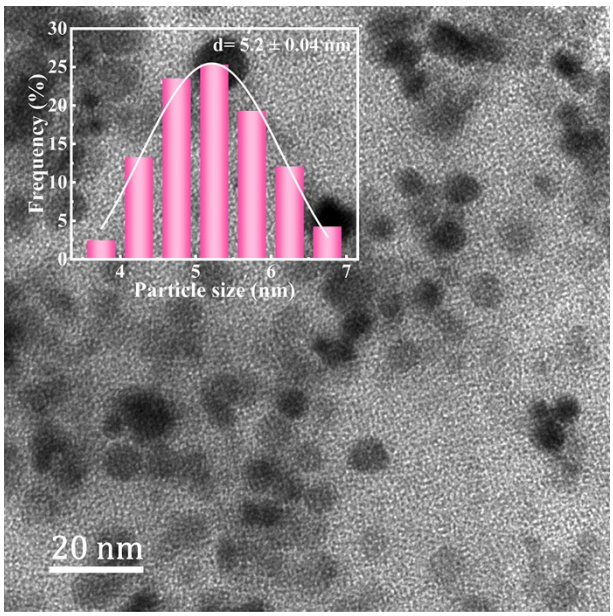

Fig. S17 TEM image and particle-size distribution of $Me_{10}CB[5]$-Sr/Pd after stability test in 0.5 M $KHCO_3$.

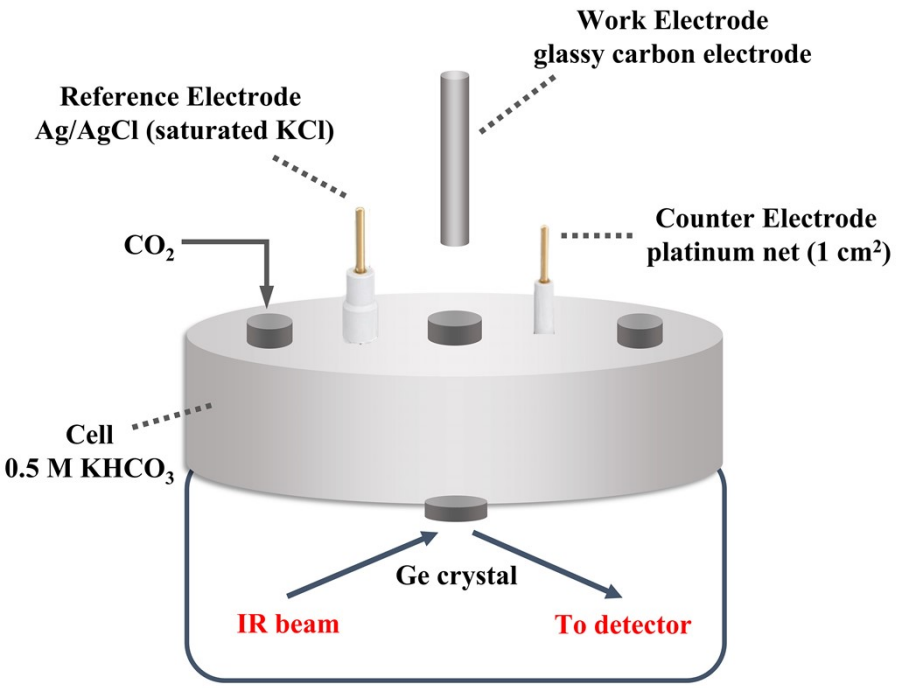

Fig. S18 The schematic illustration of operando electrochemical ATR-FTIR measurement.

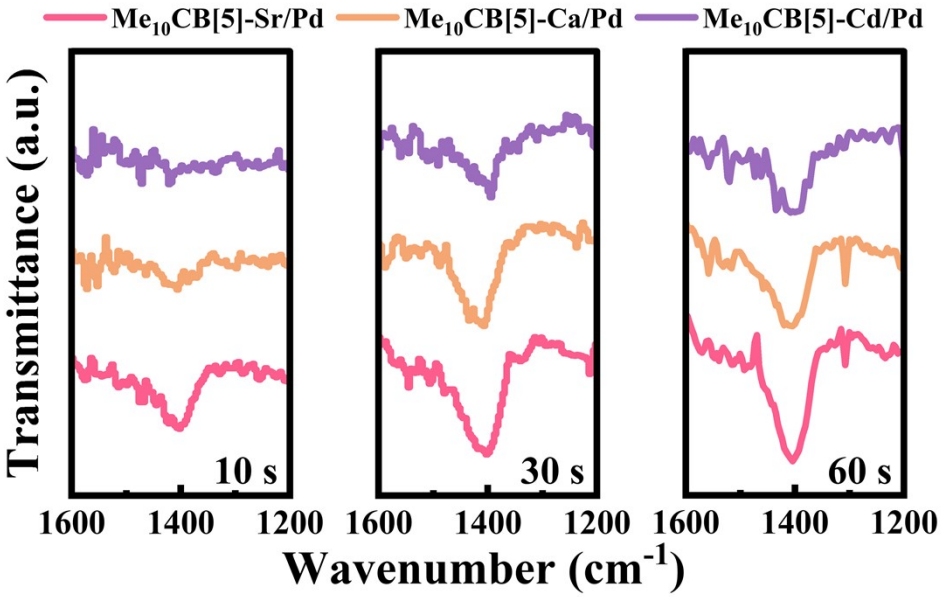

Fig. S19 Operando ATR-FTIR spectra of $Me_{10}CB[5]$-M/Pd collected at -0.7 V vs. RHE under CO_2-saturated 0.5 M $KHCO_3$ electrolyte.

Table S1: Crystallographic Data for the $Me_{10}CB[5]$-M/[$PdCl_4$].

	1	2	3
Empirical formula	$C_{40}H_{74}Cl_4N_{20}O_{22}PdSr$	$C_{80}H_{100}Cl_{21}N_{40}O_{20}Pd_4Ca_4$	$C_{40}H_{58}Cl_5N_{20}O_{13.65}PdCd$
Formula weight	1523.02	3272.37	1433.52
Crystal System	Monoclinic	Orthorhombic	Monoclinic
Space group	$P2_1/n$	Cmcm	Pbcm
a (Å)	14.0912 (8)	11.7385 (3)	11.7207 (4)
b (Å)	19.2141 (9)	29.2807 (8)	28.2643 (9)
c (Å)	21.2878 (1)	18.3247 (4)	18.5145 (5)
α (°)	90	90	90
β (°)	100.054 (2)	90	90
γ (°)	90	90	90
V (Å^3)	5675.2 (5)	6298.4 (3)	6133.4 (3)
T (K)	149.97	100	150.04
Z	4	2	4
F(000)	3128	3282	2904.8
R_{int}	0.0250	0.0764	0.0555
wR_2	0.0702	0.1939	0.1455
GOOF	1.03	1.135	0.767

Table S2: Different valence distribution of Pd for $Me_{10}CB[5]$-M/Pd.

Samples	Pd species	Binding Energy (eV) $3d_{5/2}$	$3d_{3/2}$	Relative area Peak (%)
$Me_{10}CB[5]$-Sr/Pd	Pd (0)	334.9	340.1	86.9
	Pd (II)	337.6	342.7	13.1
$Me_{10}CB[5]$-Ca/Pd	Pd (0)	334.8	340.1	78.1
	Pd (II)	336.8	342.2	21.9
$Me_{10}CB[5]$-Cd/Pd	Pd (0)	335.1	340.3	64.3
	Pd (II)	336.7	342.1	35.7

Table S3: Detail Inductive Coupled Plasma (ICP) data of Pd for $Me_{10}CB[5]$-M/Pd.

Samples	Pd (%)
$Me_{10}CB[5]$-Sr/Pd	9.46%
$Me_{10}CB[5]$-Ca/Pd	11.72%
$Me_{10}CB[5]$-Cd/Pd	8.12%

Table S4: Detail information of EIS fitting data for $Me_{10}CB[5]$-M/Pd.

The equivalent circuit used to fit the EIS data	**Sample name**	**R_s (Ω)**	**Q-Yo (F)**	**Q-n (F)**	**R_{ct} (Ω)**
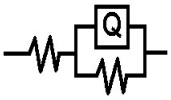	$Me_{10}CB[5]$-Sr/Pd	10.85	$1.40*10^{-3}$	0.69	44.32
	$Me_{10}CB[5]$-Ca/Pd	11.03	$1.86*10^{-2}$	0.80	56.55
	$Me_{10}CB[5]$-Cd/Pd	10.89	$1.81*10^{-2}$	0.82	131.40

Table S5: Summary of the performances of Pd-based electrocatalysts for electrochemical CO_2RR in H-type cells.

Catalyst	Electrolyte	Potential	Loading (mg cm^{-2})	FE_{CO} (%)	J_{CO} (mA cm^{-2})	CO mass activity (mA mg^{-1})	Stability (h)	Ref.
Me_{10}CB[5]-Sr/Pd	**0.5 M $KHCO_3$**	**-0.7**	**0.09**	**91.3**	**4.7**	**52.2**	**30**	**This work**
Pd-NSs	0.1 M $KHCO_3$	-0.7	0.19	93	6.6	34.7	0.8	1
C-Bi6Pd94-SAA NDs	0.1 M $KHCO_3$	-0.5	2.60	90.5	1.9	5	10	2
CuPd NPs	0.1 M $KHCO_3$	-0.9	0.04	87	~1.8	47.7	6	3
Pd-nanocubes	0.1 M $KHCO_3$	-0.9	N.R.	~78	~4.1	N.R.	N.R.	4
Pd-Me_{10}CB[5]	0.5 M $KHCO_3$	-0.6	0.12	92.5	3.98	33.1	12	5
Pd NPs	1 M $KHCO_3$	-0.7	0.40	93.4	22.9	57.5	10	6
Pd Ioctahedra/C	0.1 M $KHCO_3$	-0.8	0.44	91.1	1.8	4.1	10	7
Pd/C	0.5 M $NaHCO_3$	-0.6	0.04	50	0.3	7.5	1	8
$Pd_{85}Cu_{15}$/C	0.1 M $KHCO_3$	-0.89	0.28	86	6.9	24.5	N.R.	9
3.7 nm Pd NPs	0.1 M $KHCO_3$	0.89	0.37	91.2	8.9	23.9	N.R.	10

References:

1. Y. Zhao, X. Tan, W. Yang, C. Jia, X. Chen, W. Ren, S. C. Smith and C. Zhao, Surface reconstruction of ultrathin palladium nanosheets during electrocatalytic CO_2 reduction, *Angew. Chem. Int. Ed.*, 2020, **59**, 21493-21498.
2. H. Xie, Y. Wan, X. Wang, J. Liang, G. Lu, T. Wang, G. Chai, N. M. Adli, C. Priest, Y. Huang, G. Wu, and Q. Li, Boosting Pd-catalysis for electrochemical CO_2 reduction to CO on Bi-Pd single atom alloy nanodendrites, *Appl. Catal., B Environ.*, 2021, **289**, 119783.
3. Y. Mun, S. Lee, A. Cho, S. Kim, J. W. Han and J. Lee, Cu-Pd alloy nanoparticles as highly selective catalysts for efficient electrochemical reduction of CO_2 to CO, *Appl. Catal., B Environ.*, 2019, **246**, 82-88.
4. X. Yang, J. H. Lee, S. Kattel, B. Xu and J. G. Chen, Tuning reaction pathways of electrochemical conversion of CO_2 by growing Pd shells on Ag nanocubes, *Nano Letters*, 2022, **22**, 4576-4582.
5. R. Chen, M. Cao, W. Yang, H. Wang, S. Zhang, H. Li, and R. Cao, Ultra-small Pd nanoparticles derived from a supramolecular assembly for enhanced electrochemical reduction of CO_2 to CO, *Chem. Commun.*, 2019, **55**, 9805-9808.
6. D. Gao, H. Zhou, F. Cai, D. Wang, Y. Hu, B. Jiang, W.-B. Cai, X. Chen, R. Si, F. Yang, S. Miao, J. Wang, G. Wang and X. Bao, Switchable CO_2 electroreduction via engineering active phases of Pd nanoparticles, *Nano Res.*, 2017, **10**, 2181-2191.
7. H. Huang, H. Jia, Z. Liu, P. Gao, J. Zhao, Z. Luo, J. Yang and J. Zeng, Understanding of strain effects in the electrochemical reduction of CO_2: using Pd nanostructures as an ideal platform, *Angew. Chem. Int. Ed. Engl.*, 2017, **56**, 3594-3598.
8. W. Sheng, S. Kattel, S. Yao, B. Yan, Z. Liang, C. J. Hawxhurst, Q. Wu and J. G. Chen, Electrochemical reduction of CO_2 to synthesis gas with controlled CO/H_2 ratios, *Energy Environ. Sci.*, 2017, **10**, 1180-1185.
9. Z. Yin, D. Gao, S. Yao, B. Zhao, F. Cai, L. Lin, P. Tang, P. Zhai, G. Wang, D. Ma, and X. Bao, Highly selective palladium-copper bimetallic electrocatalysts for the electrochemical reduction of CO_2 to CO, *Nano Energy*, 2016, **27**, 35-43.
10. D. Gao, H. Zhou, J. Wang, S. Miao, F. Yang, G. Wang, J. Wang and X. Bao, Size-dependent electrocatalytic reduction of CO_2 over Pd nanoparticles, *J. Am. Chem. Soc.*, 2015, **137**, 4288-4291.